Earth and Planetary Science Letters 553 (2021) 116621

Contents lists available at ScienceDirect

Earth and Planetary Science Letters

www.elsevier.com/locate/epsl

Material failure and caldera collapse: Insights from the 2018 Kilauea eruption

Gabrielle Tepp

U. S. Geological Survey, Alaska Volcano Observatory, 4230 University Drive Suite 100, Anchorage, AK, 99508, United States of America

ARTICLE INFO

Article history:
Received 17 March 2020
Received in revised form 31 August 2020
Accepted 29 September 2020
Available online 20 October 2020
Editor: J.-P. Avouac

Keywords:
failure forecast method
caldera collapse
volcano seismology
volcano geodesy
material failure
Kilauea

ABSTRACT

The Failure Forecast Method (FFM) was introduced as an empirical model for forecasting catastrophic material failures related to natural hazards, such as landslides and volcanic eruptions, with mixed success. During the 2018 eruption of Kilauea volcano, Hawaii, the draining of the summit magma reservoir into the Lower East Rift Zone resulted in the formation of a new caldera at the summit. I tested the applicability of the FFM to caldera collapse by analyzing the cyclical earthquake swarms and ground deformation that occurred between 62 sudden major caldera collapse events. The progression of both the cumulative moment release of the cyclical earthquakes and the GNSS displacement show a major change in mid-June. In late May through early June, the progression of the parameters is consistent with strain localization or creep progression related to the development or activation of the ring fault system. From late June until the end of the eruption, parameter progression is roughly steady with initial accelerating increases in cumulative moment and displacement that shift to approximately linear progression. Analysis of repeating earthquake families in the cyclical swarms showed that the behavior of the repeaters was consistent with that of the cyclical swarms as a whole and suggested that each family undergoes its own progression of activation to termination. While the FFM analysis identified the system change in mid-June, it did not demonstrate an ability to forecast collapse events or the end of the eruption.

Published by Elsevier B.V.

1. Introduction

Material failure processes are important in many contexts, from engineering to natural hazards, and on a wide range of scales. In geosciences, the study of material failure has been applied to a variety of processes from rock fracturing to natural hazards. The introduction of the failure forecast method (FFM; e.g., Voight, 1988; Voight and Cornelius, 1991) has led to a variety of attempts to predict sudden catastrophic failure events, such as landslides (e.g., Federico et al., 2012; Carlà et al., 2017) and volcanic eruptions (e.g., Kilburn and Voight, 1998; Tárraga et al., 2008). The study of material failure can also be used to gain more insight into the processes involved in failing systems and why not all failing systems end in a catastrophic material failure (e.g., Cornelius and Scott, 1993; Sornette et al., 2004; Gershenzon, 2019).

Material failure laws have been applied to different geophysical parameters related to strain and energy release. In the context of natural hazards, these parameters are typically geodetic (e.g., ground movement, tilt, length changes) or seismic (e.g., root-mean square amplitude, earthquake rates). The success of applying the FFM to these different parameters to effectively forecast catastrophic failure events has been mixed, with limitations of the FFM noted (e.g., Cornelius and Voight, 1994; Bell et al., 2011; Boué et al., 2016; Bevilacqua et al., 2019). One reason for this may be choosing a parameter that does not accurately reflect the failure process in the given situation. Another may be the lack of understanding of the processes involved in the failure and how to evaluate if a catastrophic failure should be expected.

In early May 2018, the long-lived lava lake in Halemaumau crater at the summit of Kilauea volcano, Hawaii, began to quickly drain after a rift zone intrusion and subsequent collapse at the Pu'u 'O'o vent down-rift of the summit, marking the start of a major eruption (Neal et al., 2019). As eruptive fissures opened in the lower East Rift Zone, the summit caldera began to collapse centered near Halemaumau crater. Sudden collapse events with energy release equivalent to M5 earthquakes occurred roughly every 1-2 days starting May 17 (UTC) and were preceded by swarms of earthquakes and cycles of ground deformation (Fig. 1a). The seismic rate of the earthquake swarms increased leading up to the collapse events, with the rate dropping significantly after a collapse event occurred. From mid-May until the end of the eruption in early August, the summit crater continued to collapse and grow in size (Fig. 1b).

E-mail address: gtepp@usgs.gov.

https://doi.org/10.1016/j.epsl.2020.116621
0012-821X/Published by Elsevier B.V.

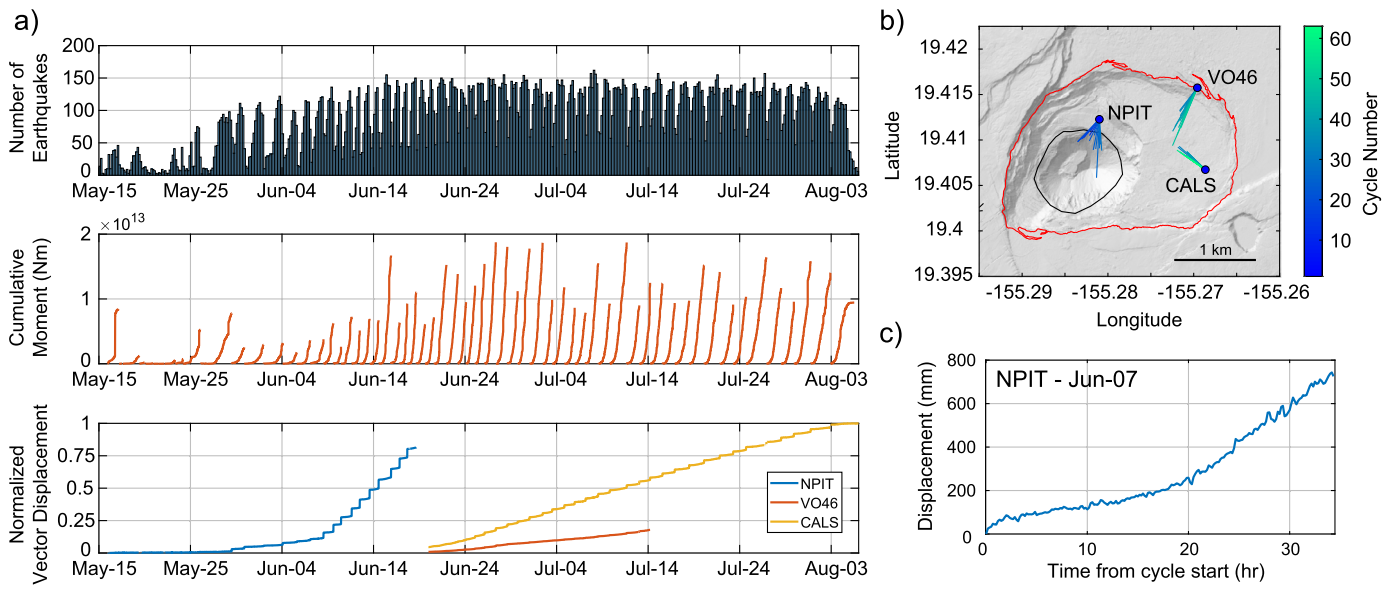

Fig. 1. Caldera collapse overview. (a) Earthquake and GNSS displacement observations over the duration of the caldera collapse. Top: Earthquake count histogram using 4-hour bins. Middle: Cumulative moment of each earthquake swarm, not including collapse events. Bottom: Normalized vector magnitude displacements from GNSS stations. (b) Map showing locations of GNSS stations used in this study. Blue-green lines show horizontal displacement during each cycle with line length proportional to total displacement. Black line shows the extent of Halemaumau crater prior to the collapse. Red line shows the boundary of the newly formed collapse caldera. (c) An example of one cycle of displacement measured by NPIT for cycle 19 starting on June 7. (For interpretation of the colors in the figure(s), the reader is referred to the web version of this article.)

The 2018 Kilauea eruption presents a unique opportunity to test the FFM on the roof collapse of a draining magma reservoir. The caldera collapse occurred over 62 repetitive cycles which also allows us to examine how the results of the FFM change over the duration of many activity cycles. This in turn provides insights into the caldera collapse process from the perspective of material failure. In this study, I chose to focus my analysis on the cumulative moment of the summit earthquake swarms that preceded collapse events. The earthquakes are closely tied to the stress build-up in the roof rock and, thus, may be linked to potential failure of the roof. I also consider the ground deformation recorded by GNSS stations close to and within the collapse caldera. These stations recorded accelerating displacement prior to the collapse events (Fig. 1c) that could be indicative of creep leading to catastrophic failure. For this analysis, I tested different FFM models with the data. Curve fitting results for both the seismic and geodetic data show a major change in mid-June that may indicate a shift from development and activation of the ring fault system to a more stable state of stick-slip motion.

2. Failure forecast method

The FFM was introduced as an empirical model to forecast the failure time of processes undergoing accelerating creep leading to failure, such as landslides or volcanic eruptions (Voight, 1988). The FFM relates the rate of a physical observable to its rate of change:

$$d^2\Omega/dt^2 = A(d\Omega/dt)^{\alpha} \quad (1)$$

where Ω is an observable parameter and A and α are constants. The parameter α is particularly important in determining the behavior of the process and whether it will lead to catastrophic failure ($\alpha > 1$). In many natural hazard situations, α is approximately 2, which is a special case where the slope of the inverse observable rate decreases linearly over time, making estimations of failure time easy (e.g., Voight, 1988). However, failure times can also be determined for any $\alpha > 1$. For the case of $\alpha < 1$, the analytical FFM solution has an infinite limit and no failure time (e.g., Cornelius and Voight, 1994). Some studies (e.g., McGuire and Kilburn, 1997; Kilburn and Voight, 1998; Kilburn, 2003) have found that α can change over time, typically moving from 1 to 2, which indicates a change in the physical system or dynamics.

The FFM has two generalized solutions: a power law ($\alpha \neq 1$) and an exponential curve ($\alpha = 1$), respectively:

$$\dot{\Omega} = (ct + b)^a \quad (2)$$

$$\dot{\Omega} = be^{at} \quad (3)$$

where $\dot{\Omega}$ is the rate of the observable, t is the time from the swarm start, and a, b, and c are constants. These equations can be integrated for the observable, Ω, and retain the same general form. The FFM parameter α can also be determined by integrating the solution for $\dot{\Omega}$ from Voight (1988) and comparing it to equation (2), giving $\alpha = (a-2)/(a-1)$. These equations are fit to the seismic and geodetic data using a least-squares method with combinations of several input parameters to assess the stability of the results.

3. Data & analysis

3.1. Seismic data

For the seismic analysis, I used the earthquake catalog from the U.S. Geological Survey Hawaiian Volcano Observatory (HVO). The catalog includes 43,773 M≥1 earthquakes between 15 May 22:35 and 2 August 21:54, which is the period when sudden collapse events occurred. I removed 499 possible duplicate events from the catalog. The magnitude of completeness is approximately 2.5 but may be a little lower for earthquakes occurring within the first third of a cycle (Supp. Fig. S1; Shiro et al., 2018). Swarms were defined as starting 5 min after a sudden collapse event and ending at the start of the next one. The first swarm had a manually chosen onset. The first 12 swarms produced much less seismicity than later ones, with 7 of the swarms in May having <90 earthquakes (range 11-51, average 23), resulting in less reliable analyses.

The progression of earthquake swarms is often characterized in different ways, such as with earthquake rates and cumulative moment. Fig. 2 shows how earthquake rate, average magnitude, and cumulative moment progressed for all cycles. The earthquake rate

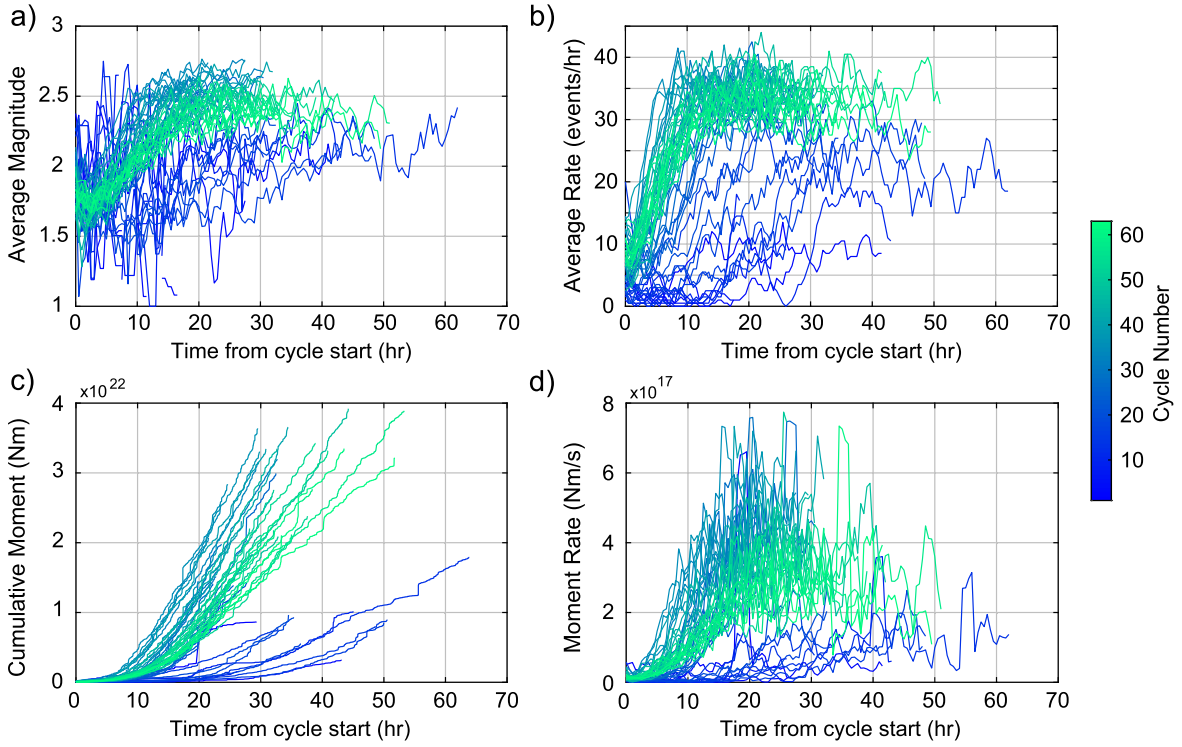

Fig. 2. Progression of earthquake swarm parameters for all cycles: (a) average magnitude, (b) average earthquake rate, (c) cumulative moment, and (d) moment rate. (a), (b), and (d) were calculated using 2-hr windows with 1.5 hrs of overlap. Partial lines in (a) result from windows with no earthquakes.

increases for the first ∼10 hours before leveling off, likely due to saturation of the catalog during high rate activity. The average magnitude continues to increase for longer, ∼20 hours, before the rate of increase slows or stops. The progression of the average magnitude is more likely related to physical changes in the system than a detection issue. To minimize issues with catalog completeness, I chose to analyze the cumulative moment which should not be strongly affected by missing small magnitude events during periods of high earthquake rates when average magnitudes are larger. The cumulative moment is calculated from the local magnitude using the relation determined by Zúñiga et al. (1988) for Hawaii, with magnitude errors shown in Supplementary Figure S2. For the curve fitting, I used 180 combinations of initial parameters for the power law (equation (2)) and 35 for the exponential (equation (3)).

The cumulative moment was best fit by the power law, although the exponential also provided good fits for some of the earlier cycles (Figs. 3a & 4a). Prior to about June 20, the a-values were fairly variable with most near 3-4 (mean 4.8 ± 3.1, median 3.1 starting May 29). After this, the a-values became more stable around 2-2.5 (mean 2.2 ± 0.2, median 2.2). The estimates of α are between 0.5-1 prior to June 14 when they begin to decrease to around ∼0.25, by approximately June 20. This is consistent with the exponential fits ($\alpha = 1$) being better in earlier cycles.

Given the change in character of the swarms with time (Fig. 2), I also tested the power law on each part of the cycles, divided at the time the average magnitude became approximately steady. For the first part of the cycles (Fig. 4b), the α-values progressed similarly to those of the full cycle fits but with values around 0.5 higher. Between May 28 and June 10, α-values had a mean of 1.1 ± 0.2. They became more variable between 0.5-1.25 (mean 0.9 ± 0.3) until about June 24 when they decreased to a mean of 0.6 ± 0.2. Given the α-values near 1, I also tested exponential fits (Fig. 3b). These provided better fits than the power law, and the earlier swarms were generally better fit than later swarms, similar to the power law. The second parts of the cycles were fit best by a line ($a = 1$; Fig. 3c), though there is some deviation from this, especially for earlier cycles (e.g., May, early June).

3.1.1. Repeating earthquake families

Given the complexity of caldera collapse, it is reasonable to assume that multiple processes and source locations are producing earthquakes during any single swarm. To separate different sources, earthquakes can be correlated and sorted into families of highly-correlated earthquakes (typically those with correlation values >0.7 in volcanic regions; e.g., Minakami et al., 1951; Green and Neuberg, 2006; Uchida and Bürgmann, 2019; herein "repeaters"). Repeaters are assumed to have a highly similar, non-destructive source location and mechanism and have different characteristics (e.g., rate variation, magnitude range) depending on the source process. Thus, each repeater family can be considered to represent a single fault or non-fault source, allowing one source to be analyzed at a time for the presence of a failure process (e.g., Salvage and Neuberg, 2016).

During the 2018 Kilauea eruption, repeater families occurred both near the boundaries of the collapse caldera and within it, with many families active over multiple cycles (Shelly and Thelen, 2019). The percentage of earthquakes that were repeaters significantly increased during the first ∼20 cycles, and the most active locations for repeaters also varied over the eruption duration (Tepp et al., 2020). I applied the FFM analysis to the 13 families with the most repeaters (305-1020 total) and for cyclical swarms within each family that have at least 10 repeaters in order to have enough data points for reliable curve fitting. I used the catalog of Shelly and Thelen (2019), which is a more complete catalog of repeating earthquakes than the HVO catalog, associated with repeater families found by the REDPy algorithm (Hotovec-Ellis and Jeffries, 2016; A. Hotovec-Ellis, written pers. comm., 2019). This associated catalog included 26,932 repeaters within my analysis period. I applied power law fits to the cumulative moment of each swarm to estimate α (Fig. 5).

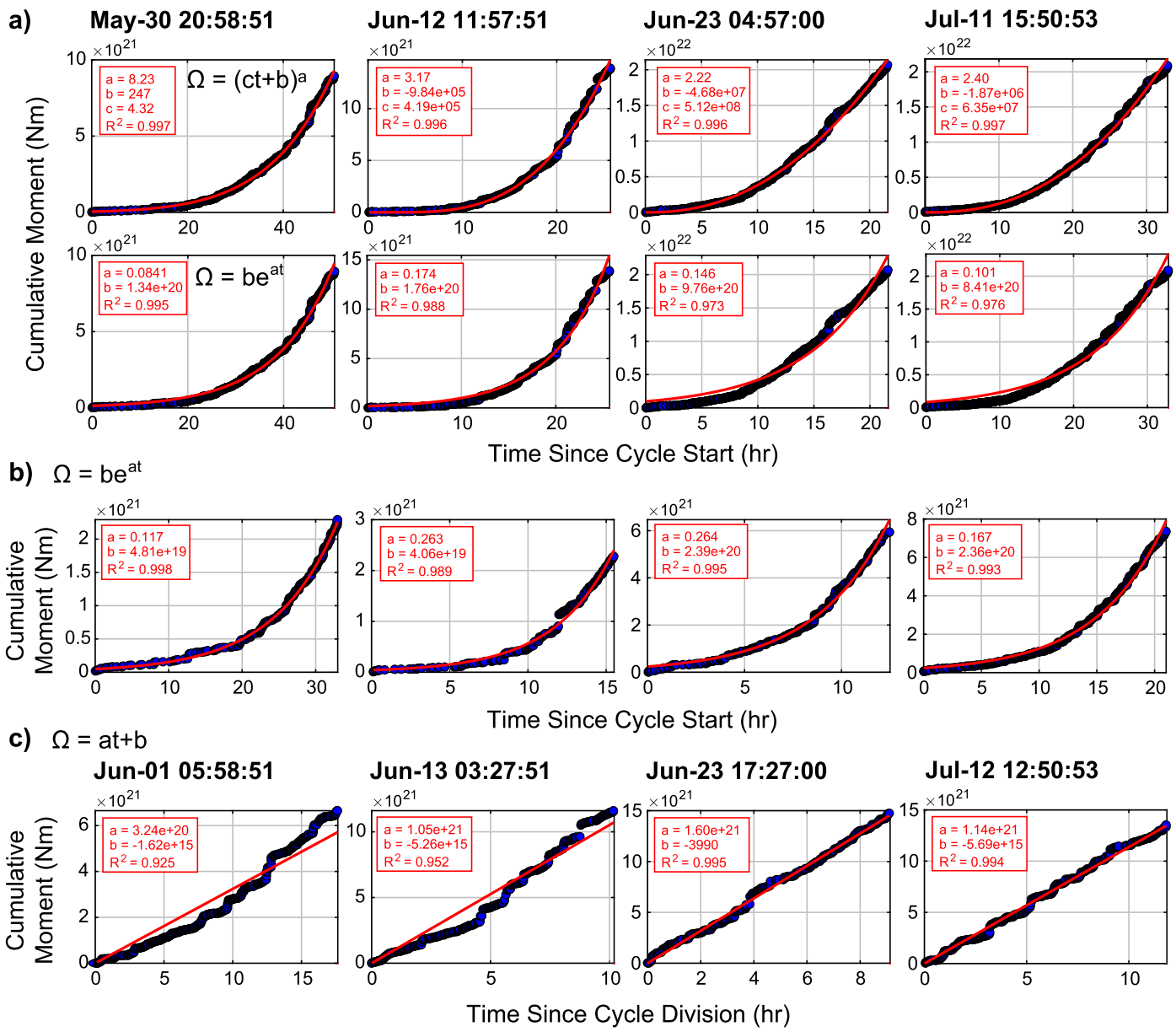

Fig. 3. Examples of fits to cyclical earthquake swarms. (a) Power law (top) and exponential (bottom) fits to the full cycle. (b) Exponential fits to the first part of the cycle. (c) Linear fits to the second part of the cycle. Blue circles show cumulative moment, and red lines are the curve fit.

The estimated α-values cover a wide range; however, most are $<\sim 1$ (with a-values typically between 1.5 and 3.5). The cumulative moment of many families was roughly linear or variable. A few families (827, 1332, 1985, 3331) included a few swarms that did have clear power law (or exponential) shapes. Family 827 was the most interesting, having several early swarms with α-values near 0.9. Several of the families had decreasing α-values, usually earlier in the sequence. Only one (277) showed a clear increase, although most of its swarms were close to linear. For the 5 families occurring at least partially in mid-June, α-values were mostly steady until around June 20 when they began to decrease. This is most clear for the 4 families near the eastern collapse boundary. Three later families (near the north and south collapse boundaries) also show this pattern in late June-late July.

The repeater results are mostly consistent with the results from the analysis of all earthquakes. Shelly and Thelen (2019) noted that different repeater families started at different times within a single cycle. The curvature or linearity of the repeater swarms did appear to match with that of the full swarms, with repeater swarms that started later in cycles having a more linear cumulative moment. This suggests that their overall behavior was controlled by the same process as the full swarms. For several of the families, there was a subtle shift in the shape of the cumulative moment over the sequence of swarms. The earlier swarms were approximately linear, but later swarms started linear then slowed down near the end of the cycle. The upward curving (i.e., power law or exponential) swarms also almost always appeared earlier in the sequence. This suggests that each repeater location had its own progression from formation or activation to cessation of activity.

3.2. Geodetic observations

I examine displacement data from 3 GNSS stations located within the region affected by the caldera collapse. These stations mostly had increasing displacements leading into the collapse events. The horizontal vectors varied in direction throughout the eruption sequence (Fig. 1b) but were nearly always consistent within a single cycle. Two stations, NPIT and VO46, were situated

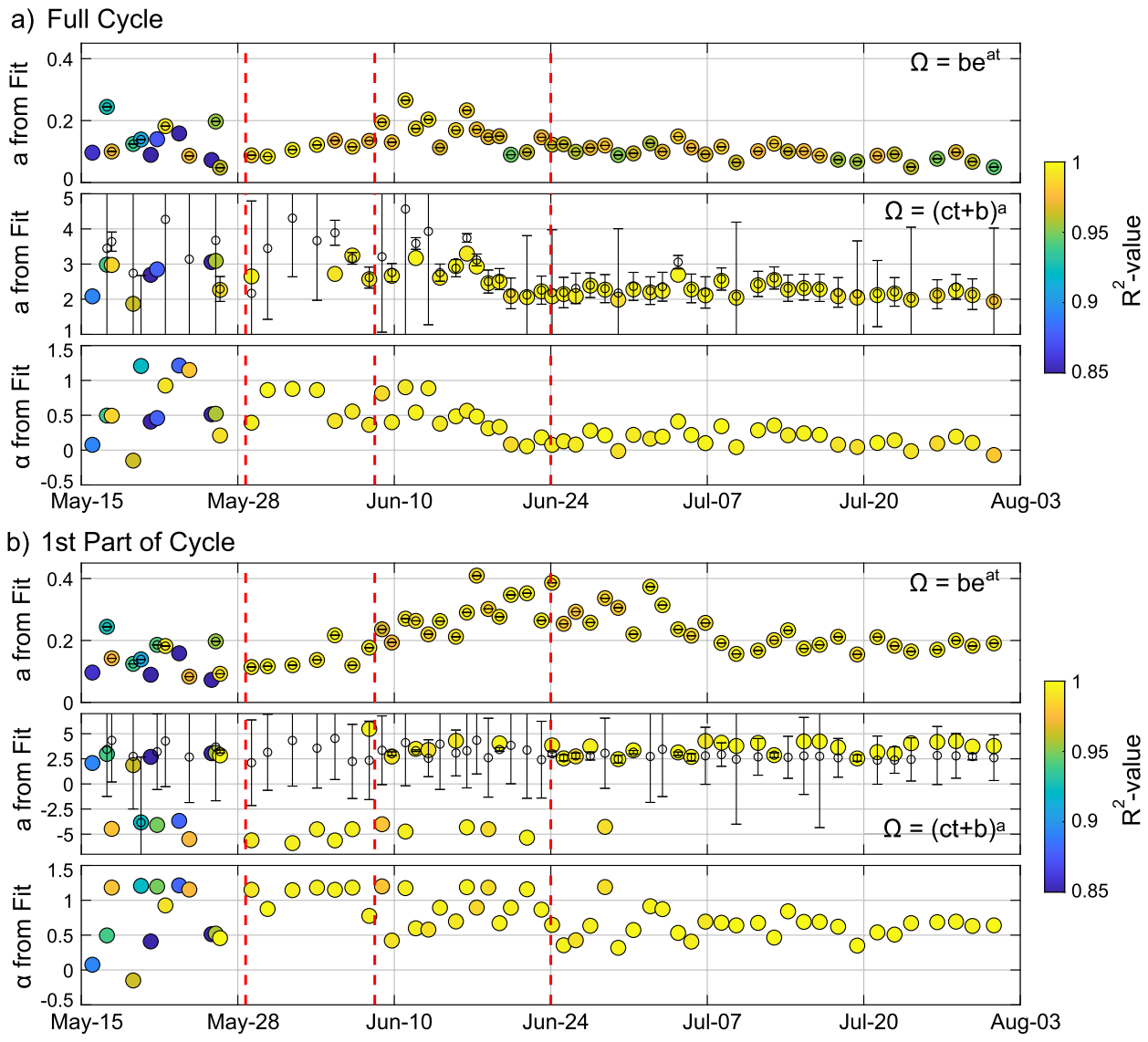

Fig. 4. Curve fitting results for cyclical earthquake swarms. Fits to (a) the full cycle and (b) the first half of each cycle. Parameter a from (top) the exponential fits (equation (3)) and (middle) the power law fits (equation (2)) colored by the R^2 value of the fit (higher is better). (bottom) Values of α determined from the power law exponent colored by the R^2 value of the power law fit. The colored circles show the value from the best fit. The median of the 20 highest-R^2 fits (or all fits with $R^2 \geq 0.9$) are shown as open markers with lines indicating the standard deviation. Red dashed lines indicate times of major changes in the collapse progression from Tepp et al. (2020).

very near the growing caldera rim (Fig. 1b) and were affected by cliff collapses that stopped data return after 29 cycles (ending on June 18) and 19 cycles (starting June 20), respectively. The station CALS was situated within the new caldera starting on June 20 and recorded through the end of the eruption. I averaged 5-second, real-time-processed displacement solutions from HVO in 10-minute, non-overlapping windows to reduce noise. The displacement errors are shown in Supplementary Figure S3. I fit the generalized power law solution (equation (2)) to the vector magnitude of the horizontal components of displacement, the vertical displacement, and the 3-dimensional vector magnitude to evaluate the evolution of displacement and whether there is variation based on the components (Fig. 6). Fitting was done with 320 combinations of initial parameters.

For the cycles that are well fit by the power law, the a-values of both CALS and VO46 typically fell within the range of 1.2-3 with medians of 2 and 1.7, respectively (Fig. 7a). The a-values for NPIT had a similar median of 2.3 but were much more variable, ranging from −34 to 15. Most of the first 12 cycles have low amplitude and are strongly affected by noise, so I exclude them from interpretations. Cycles 10 (May 24) and 13-15 (May 26-30) are also fairly noisy, but reasonable fits are possible. The horizontal and vertical displacements for all stations had similar a-values to those for the 3-d displacements. For cycles that were well fit by the FFM model, the a-values of the top 20 fits with $R^2 \geq 0.9$ had little variability, indicating that the values are reliable. Fig. 7b shows the α-values estimated from the best 3-d displacement fits. Several cycles on NPIT prior to June 10 have α-values close to 1, after which they decrease toward 0. These cycles were not well fit by the power law and produced highly variable fit parameters (Figs. 6 & 7).

As can be seen in Figs. 1c & 6, the displacement behavior in some cycles is reminiscent of the creep curve from material failure (e.g., Chandler, 1991; Main, 2000), suggesting that there may be clear stages of primary, secondary, and tertiary creep. Main (2000) introduced a hybrid model to fit the behavior of these curves:

$$\Omega = c * (1 + t/b)^a + f * (1 - t/e)^{-d} \quad (4)$$

Where a, b, c, d, e, and f are positive parameters with $a < 1$. The first term relates to the initial stage of primary creep, and the second term describes the tertiary (accelerating) creep stage with

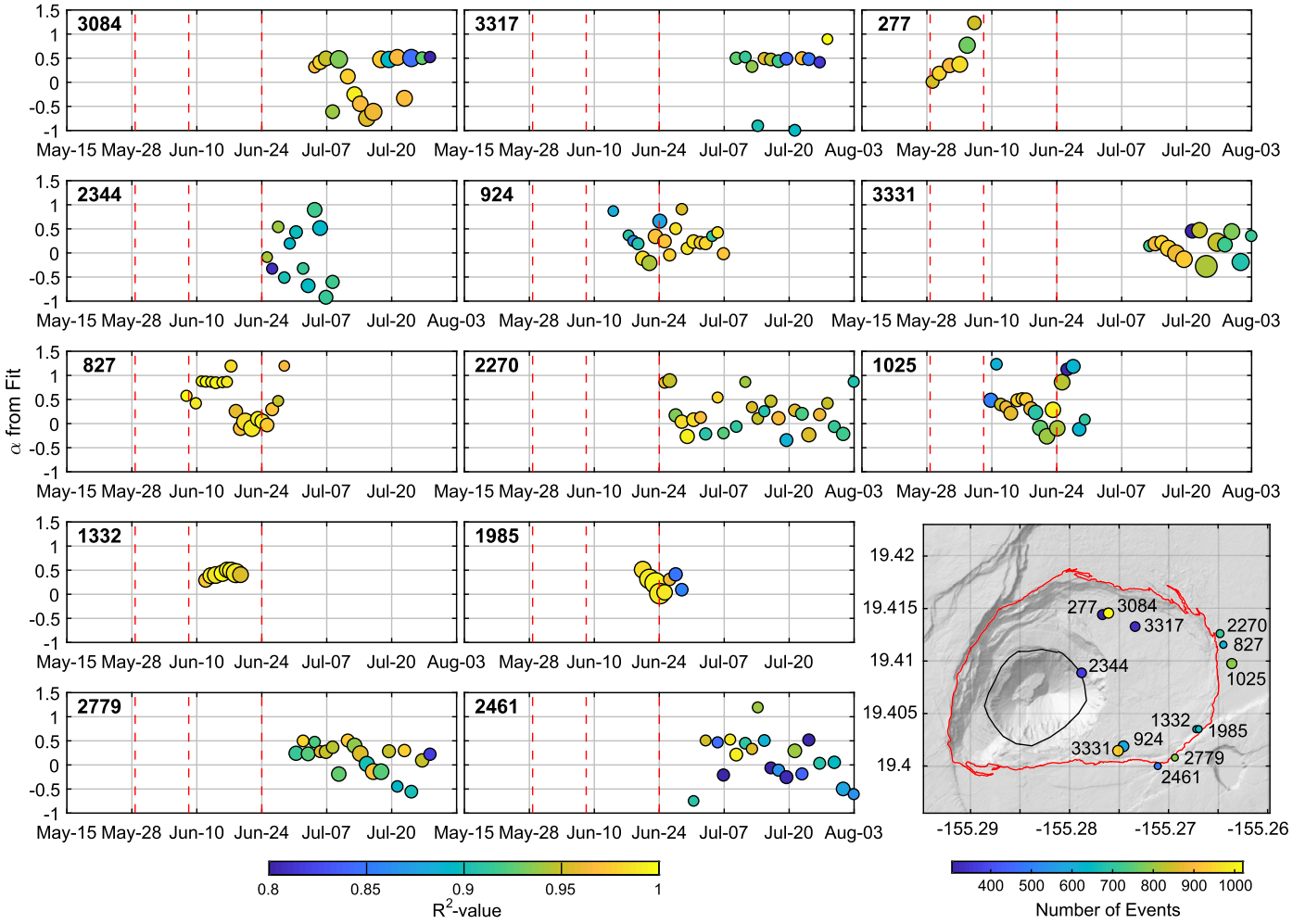

Fig. 5. Curve fitting results for repeating earthquake families with at least 300 total earthquakes. Scatter plots show α-values estimated from FFM fits for cyclical swarms within each family that have at least 10 earthquakes. Marker sizes scale with the number of earthquakes in the swarm. The number of the family is given in the top left corner of each plot with the corresponding average family location marked on the map. Map marker sizes scale with depth (bigger is deeper). Red dashed lines indicate times of major changes in the collapse progression from Tepp et al. (2020).

e equal to the failure time. I apply this model to the 3-d displacement data to see if the fits improve from the power law. I used 576 combinations of initial parameters for the fits. Fig. 8 shows the exponents (a&d) and failure time (e) parameters from the fits, considering only those that meet the parameter constraints (all positive, $a < 1$) and have a failure time between a factor of 1/2 and 2 of the real failure time. Removing the failure time constraint gives very similar fits but with more variability in the parameters. Equation (4) fits well to the NPIT data, but fits worsen after about June 10. The CALS and VO46 data are not as well fit by equation (4); however, if the equation is rewritten with all positive values (i.e., letting d and e be negative), the fits improve, particularly for cycles that have an initial bump, but remain comparable to or slightly worse than the power law fits. In this case, the simpler power law fit is preferred to avoid potential over-fitting.

4. Discussion

The value of α provides insight into the processes controlling the observable, Ω. For many natural hazards, α is found to be around 1 or 2 (e.g., Voight, 1988; Cornelius and Voight, 1994; Kilburn and Voight, 1998). When considering seismicity, Kilburn and Voight (1998) suggest that for low strain rates, α approaches 1 and the formation of new cracks are the dominant fracturing process whereas for higher strain rates, α approaches 2 and the fracturing rate is controlled by crack growth. During system failures, α can change over time, typically moving from 1 toward 2 as cracks grow and coalesce (Kilburn, 2003). Values of $\alpha < 1$ may result from sparse data (Cornelius and Scott, 1993) or non-failure processes. For most full cycles of both the cumulative moment and displacement, α-values are <1 and not meaningful within the FFM framework. Thus, they require a little more consideration. An observable with $a = 2$ ($\alpha = 0$) has constant acceleration, whereas an observable with $a = 1$ ($\alpha \to -\infty$) has no acceleration. Between these values, the acceleration is initially large but quickly decreases (e.g., for $a = 1.5$, acceleration decreases as $t^{-1/2}$). For $a > 2$, acceleration increases, and α is a positive value <1.

For the Kilauea caldera collapse, the a (or α) values for both the cumulative moment and displacement changed over the course of the eruption, most notably decreasing in mid-June, suggesting one or more changes in the system around that time. While both displacement and cumulative moment can be used as proxies for strain (e.g., Voight, 1988; Main, 1999), they may also be indicative of different processes or parts of the system. This is important to keep in mind while interpreting the results.

Most conceptual models of caldera collapse rely on a piston mechanism wherein a central piston forms above the magma reservoir and then sinks in a series of drops that generate large magnitude, very-long-period seismic signals (e.g., Kumagai et al., 2001). Ruch et al. (2012) performed analog experiments to evalu-

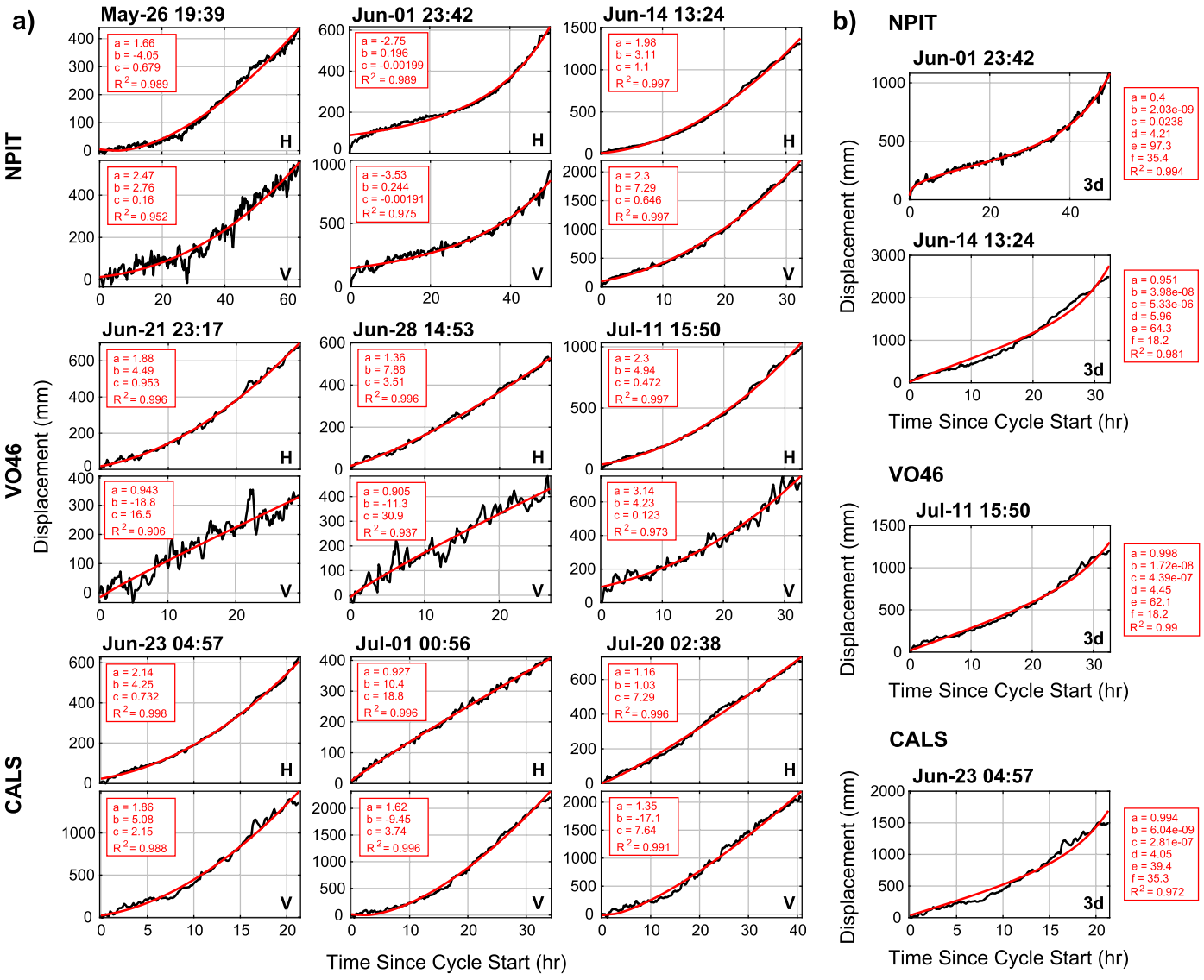

Fig. 6. Example fits to GNSS data. (a) Power law fits (red) to the horizontal (H) and vertical (V) magnitudes of displacement (black). (b) Equation (4) fits to the 3-dimensional vector magnitude of displacement.

ate how collapses happen. They found that incremental collapse, such as observed during the 2018 Kilauea eruption, occurs once ring faults surrounding the piston are established. From the surficial footprint of the Kilauea collapse, it seems likely that pre-existing western and southern bounding faults were reactivated, but it is less clear whether faults were pre-existing along the eastern boundary. Thus, one question is whether there is evidence for the formation of ring faults (i.e., "failure" of the roof rock) or whether the collapse was entirely incremental stick-slip on pre-existing ring fault structures. The change in the cyclical evolution of the displacement and cumulative moment in mid-June may indicate a progression from ring fault development to incremental stick-slip.

The first 12-13 cycles (mid to late May) were not well fit by the power law or exponential curves, likely in part from often weak seismicity or displacement, so I do not attempt to interpret the results. Numerical and analog models of caldera collapse suggest that early ring fault development begins at depth (i.e., near the magma reservoir), which may explain the weak deformation at the surface and low seismicity (e.g., Roche et al., 2000; Holohan et al., 2015). Additionally, Fontaine et al. (2019) noted very-long-period seismic signals during the 2007 Piton de la Fournaise collapse that they interpreted as collapse at depth prior to the onset of collapse visible at the surface. For Kilauea, it seems reasonable to conclude that ring fault development and collapse was occurring at depth during May. The first observations of large-scale collapse at the surface were noted on May 29 with subsidence to the north and west (Neal et al., 2019; Anderson et al., 2019), indicating that the system had reached the later stages of ring fault development.

The displacement and cumulative moment of cycles beginning on May 29 to roughly June 9 typically had α-values close to 1, consistent with fracturing and development of the ring fault system. The percentage of earthquakes that were repeaters also greatly increased during this period (e.g., Tepp et al., 2020), further evidence that seismic sources were being established. During this period, the GNSS displacements were best fit by equation (4), the model for creep curves defined by Main (2000). The displacement measured by NPIT in late May and early June could be interpreted as an accelerating failure process or strain localization, moving through all 3 stages of creep as the southern and eastern components of the ring faults were formed or reactivated. The cumulative moment also showed this character during a few cycles (e.g., May 29, June 9), though it was most noticeable on cycles where it was less present in the displacement. Tepp et al. (2020) suggest

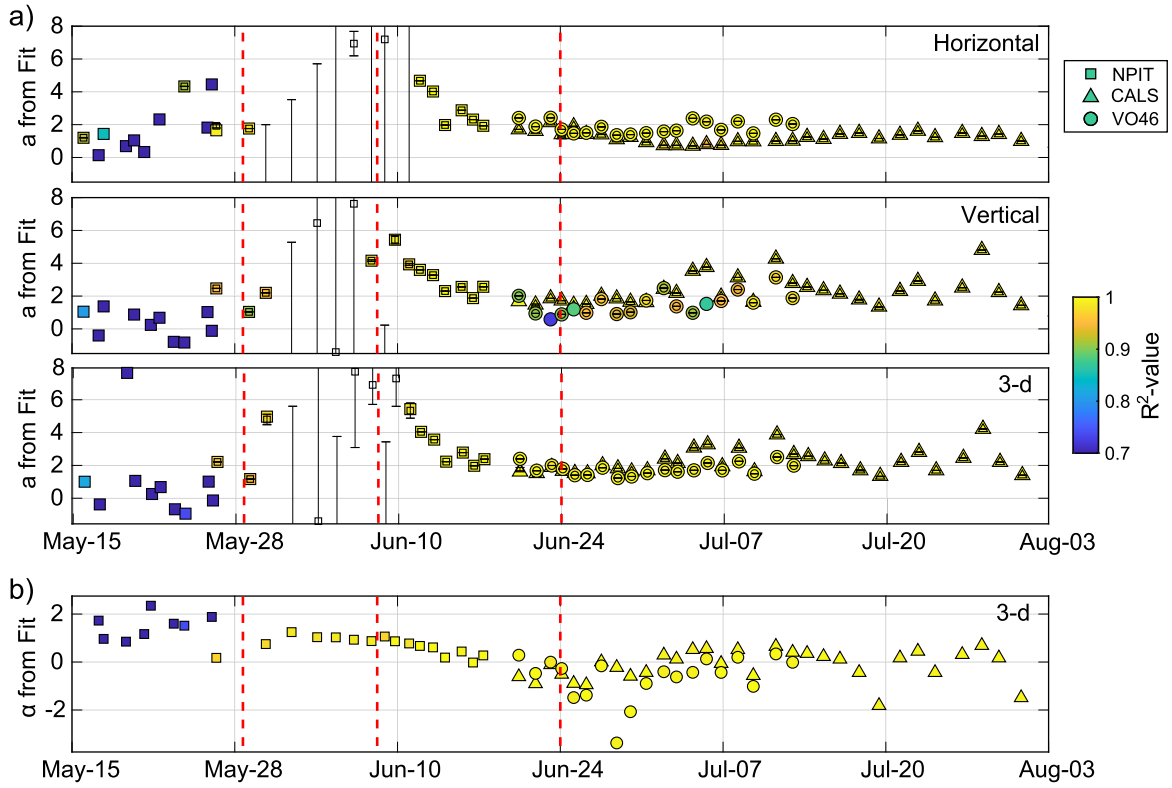

Fig. 7. Results from the FFM solutions applied to GNSS displacement data. (a) a-values of fits for the horizontal vector displacement (top), vertical displacement (middle), and 3-dimensional vector displacement (bottom). a-values of the best fits are shown as colored markers. The median of the 20 highest-R^2 fits (or all fits with $R^2 \geq 0.9$) are shown as open markers with lines indicating the standard deviation. Values beyond bounds not shown for several cycles recorded by NPIT that were not well fit by the FFM model. (b) α-values estimated from a-values of the best fits to the 3-d displacement. Red dashed lines indicate times of major changes in the collapse progression from Tepp et al. (2020).

that the main ring faults defining the piston were fully formed or reactivated around June 8, based on changes in the seismic and geodetic observations.

In mid-June (between approximately June 9 and 20-24), the α-values of displacement and cumulative moment decreased. The decrease of α-values is opposite what other studies have observed and may reflect a shift toward stability of the system rather than a growing instability. Geodetically, this period was mostly recorded by NPIT, on the western side of the collapse, whereas the earthquakes more commonly occurred on the eastern side. Since the displacement α-value decrease started and ended earlier than that of the cumulative moment, the western boundary faults may have activated earlier or more quickly than the eastern ones, perhaps unsurprisingly if they were indeed pre-existing. Fildes et al. (2020) also noted changes in several parameters of the seismicity during this time.

Starting around June 20-24, the α-values became steady around ~0.5 with less variability. During this period, both the displacement and cumulative moment seemed to take on a more linear shape, especially in the later part of each cycle (Figs. 3 & 6). At this point, the ring fault system was developed to the point that the central piston could undergo a relatively stable stick-slip movement. The initial acceleration of the piston as it began to drop resulted in accelerating cumulative moment release and displacement, but the acceleration decreased as the cycle progressed, shifting the observables to an approximately linear character. The decrease in acceleration was most likely controlled by friction on the ring faults. Pressure changes in the magma reservoir could also have contributed, but given the eventual sudden drop of the piston, it seems less likely that pressure would be the main factor in slowing the piston's acceleration.

CALS and VO46 recorded at the same time from the eastern side of the collapse caldera but from inside and outside the collapse, respectively (Fig. 1b). For the first several cycles, the displacement of both stations had similar a-values (i.e., progressed similarly) but began to separate around July 1, most notably for the horizontal and 3-d displacements (Fig. 7a). This observation suggests that the ground motion at those locations became disconnected. The separation began as the surface expression of the eastern collapse boundary became apparent (June 22-30) along with other changes that Tepp et al. (2020) interpreted as the formation of a secondary ring fault that defined a separate block on which CALS was located. The independent tilting motion of this block could explain the differences in the CALS and VO46 displacements after July 1 and the relatively high variation in CALS displacement a-values. The α-values of the cumulative moment in the first part of the cycles was also variable until around July 7, after which they became steady, indicating that late June changes in the system were also reflected in the cumulative moment. The changes in the observables in late June, however, were more subtle, suggesting that any change in the system was relatively minor compared to that in mid-June.

The seismicity, as described by cumulative moment release, appears more indicative of stress build-up in and around the collapse region than accelerating failure of the ring faults. Other studies have reached similar conclusions. Shelly and Thelen (2019) found no spatiotemporal trend in the occurrence of the earthquakes which might be expected for a propagating fault, although many earthquakes did appear to occur on the ring faults and could be related to fault creep during the stick-slip movement of the piston. They also noted a spatial difference in locations of the cyclical earthquakes and the hypocenters of the collapse events,

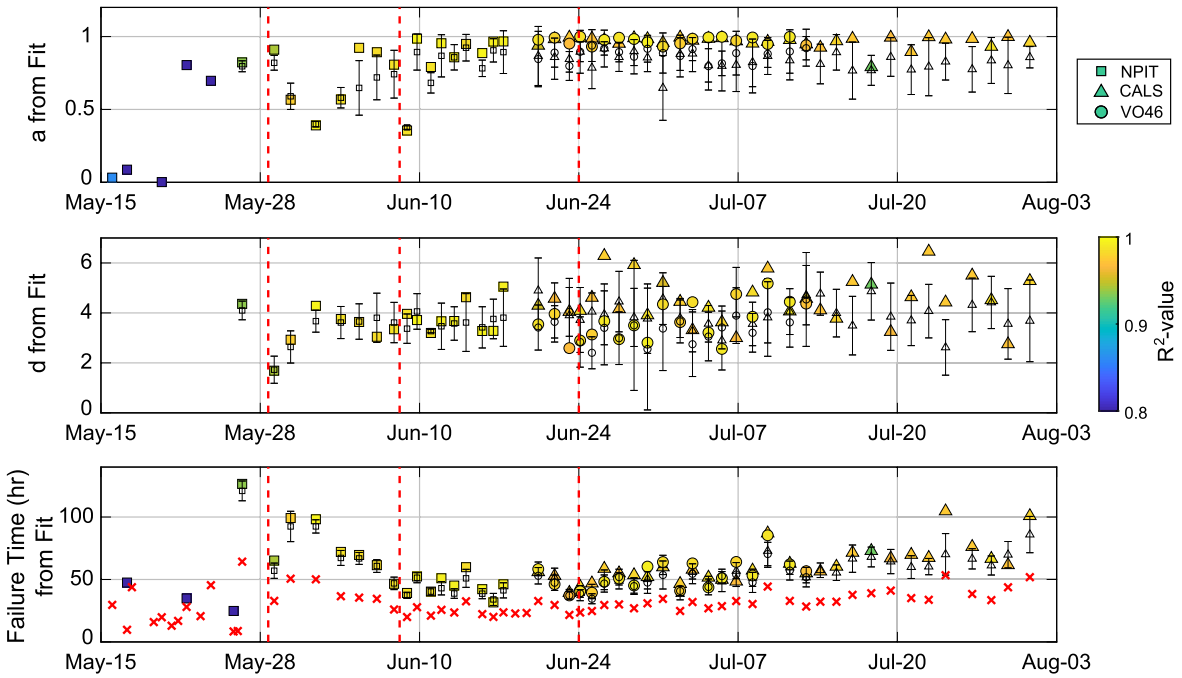

Fig. 8. Results from equation (4) fit to GNSS displacement data: exponents a (top) and d (middle) and failure time e (bottom). Values of the best fits are shown as colored markers. The median of the 20 highest-R^2 fits (or all fits with $R^2 \geq 0.9$) are shown as open markers with lines indicating the standard deviation. Values beyond bounds not shown for several early cycles recorded by NPIT. Red crosses are the times of collapse events (i.e., failure). Red dashed lines indicate times of major changes in the collapse progression from Tepp et al. (2020).

consistent with an interpretation that there was no direct relation between the two as might be expected for accelerating failure of a fault. Butler (2020) aimed to determine whether the cyclical earthquakes were foreshocks or aftershocks to the M5 collapse events and found that they fit neither of those categories. For the caldera collapse of Miyakejima in 2000, Kobayashi et al. (2003) analyzed small earthquake swarms that occurred before 4 collapse events and concluded that they resulted from stress accumulation along a shallow part of the piston. Though the character and prevalence of these swarms was much different than the Kilauea collapse swarms, the explanation of Kobayashi et al. (2003) for their occurrence is similar.

The only other seismically-recorded caldera collapse with significant non-collapse-event earthquake activity at the summit was the 1968 collapse of Fernandina, Galapagos (e.g., Simkin and Howard, 1970; Filson et al., 1973). Both the Fernandina and Kilauea collapses were determined to occur with a low roof aspect ratio (height/width) of less than one (e.g., Simkin and Howard, 1970; Anderson et al., 2019; Tepp et al., 2020). Other collapses that were well-recorded seismically (e.g., Bardarbunga, Gudmundsson et al., 2016; Miyakejima, Kumagai et al., 2001; Geshi et al., 2002; Kobayashi et al., 2003; Piton de la Fournaise, Michon et al., 2007; Staudacher et al., 2009) had higher aspect ratios and less summit earthquake activity other than the large magnitude seismic events related to collapses. If the non-collapse-event earthquakes are indeed a stress response of the shallow edifice, this may explain why microseismicity is more common among collapses with low roof aspect ratios. The shallower, broader magma reservoir may result in more critical stressing of the brittle rock of the shallow volcanic edifice, leading to more earthquake activity.

5. Summary

I applied the FFM to cyclical earthquake swarms and ground deformation data from the 2018 Kilauea caldera collapse to test its applicability to the failure of magma reservoir roofs and to examine whether changes in the system over the 62 repetitive cycles were reflected in the FFM parameters. The cumulative moment release and GNSS displacements showed both similarities and differences. Both appear indicative of the overall stress state of the system but may be reflecting different locations or processes. The α-values of the displacement and cumulative moment both start near 1 before decreasing in mid-June. This suggests that the ring fault system was developing, in terms of fault reactivation or formation, through early June after which it shifted toward a state of steady stick-slip motion. This is further supported by displacement curves that were well-fit by a creep curve model in early June and later by a near-linear power law. Once the steady state of the system was reached in late June or early July, there was no obvious change indicating the end of the eruption. An analysis of individual repeater families produced similar results to the analysis with all earthquakes and suggested that each repeater family undergoes its own sequence of activation to termination.

While my analysis of cyclical cumulative moment and deformation was able to identify the major system change in mid-June, it was not able to be used for forecasting individual collapse events at the end of each cycle or the end of the eruption as a whole. Unlike previously studied eruptions or other failure events, the α-values decreased over the sequence of cycles rather than increased, suggesting that the caldera collapse process at Kilauea moved toward a state of stable change (i.e., stick-slip). A similar analysis of non-incremental collapses could shed light on whether some modes of collapse do occur as an unstable process leading to failure of the roof.

CRediT authorship contribution statement

Gabrielle Tepp: Conceptualization, Formal analysis, Investigation, Software, Visualization, Writing - original draft, Writing - review & editing.

Declaration of competing interest

The authors declare that they have no known competing financial interests or personal relationships that could have appeared to influence the work reported in this paper.

Acknowledgements

I thank Andrea Bevilacqua for helpful discussions and Matt Haney for helpful comments on the original version of the manuscript. Many thanks to Andrew Bell, Nico Fournier, and Wendy McCausland for their very thoughtful and constructive reviews. Thanks to Ingrid Johanson and HVO for the GNSS solutions and Alicia Hotovec-Ellis for the REDPy repeater catalog. The HVO earthquake catalog is available at http://earthquakes.usgs.gov or by contacting HVO. GNSS data are available from the UNAVCO archive (https://www.unavco.org/data/gps-gnss/gps-gnss.html). Curve fitting was done using the EzyFit Toolbox for Matlab. G. Tepp was funded through the USGS Mendenhall Fellowship program. Any use of trade, firm, or product names is for descriptive purposes only and does not imply endorsement by the U.S. Government.

Appendix A. Supplementary material

Supplementary material related to this article can be found online at https://doi.org/10.1016/j.epsl.2020.116621.

References

Anderson, K.R., Johansson, I.A., Patrick, M.R., Gu, M., Segall, P., Poland, M.P., Montgomery-Brown, E.K., Miklius, A., 2019. Magma reservoir failure and the onset of caldera collapse at Kīlauea Volcano in 2018. Science 366, 6470.

Bell, A.F., Naylor, M., Heap, M.J., Main, I.G., 2011. Forecasting volcanic eruptions and other material failure phenomena: an evaluation of the failure forecast method. Geophys. Res. Lett. 38 (15).

Bevilacqua, A., Pitman, E.B., Patra, A., Neri, A., Bursik, M., Voight, B., 2019. Probabilistic enhancement of the failure forecast method using a stochastic differential equation and application to volcanic eruption forecasts. Front. Earth Sci. 7, 135. https://doi.org/10.3389/feart.2019.00135.

Boué, A., Lesage, P., Cortés, G., Valette, B., Reyes-Dávila, G., Arámbula-Mendoza, R., Budi-Santoso, A., 2016. Performance of the 'material failure forecast method-'in real-time situations: a Bayesian approach applied on effusive and explosive eruptions. J. Volcanol. Geotherm. Res. 327, 622–633.

Butler, R., 2020. Volcanic earthquake foreshocks during the 2018 collapse of Kīlauea Caldera. Geophys. J. Int. 220 (1), 71–78.

Carlà, T., Intrieri, E., Di Traglia, F., Nolesini, T., Gigli, G., Casagli, N., 2017. Guidelines on the use of inverse velocity method as a tool for setting alarm thresholds and forecasting landslides and structure collapses. Landslides 14 (2), 517–534.

Chandler, H.D., 1991. Creep modelling using semiempirical deformation and damage equations: fcc metals. Mater. Sci. Eng. A 131 (2), 177–185. https://doi.org/10.1016/0921-5093(91)90394-3.

Cornelius, R.R., Scott, P.A., 1993. A materials failure relation of accelerating creep as empirical description of damage accumulation. Rock Mech. Rock Eng. 26 (3), 233–252.

Cornelius, R.R., Voight, B., 1994. Seismological aspects of the 1989–1990 eruption at Redoubt Volcano, Alaska: the Materials Failure Forecast Method (FFM) with RSAM and SSAM seismic data. J. Volcanol. Geotherm. Res. 62 (1–4), 469–498.

Federico, A., Popescu, M., Elia, G., Fidelibus, C., Internò, G., Murianni, A., 2012. Prediction of time to slope failure: a general framework. Environ. Earth Sci. 66 (1), 245–256.

Fildes, R.A., Kellogg, L.H., Turcotte, D.L., Rundle, J.B., 2020. Interevent seismicity statistics associated with the 2018 quasiperiodic collapse events at Kīlauea, HI. Earth Space Sci. 7 (3).

Filson, J., Simkin, T., Leu, L., 1973. Seismicity of a caldera collapse: Galapagos Islands 1968. J. Geophys. Res. 78 (35), 8591–8622. https://doi.org/10.1029/JB078i035p08591.

Fontaine, F.R., Roult, G., Hejrani, B., Michon, L., Ferrazzini, V., Barruol, G., et al., 2019. Very-and ultra-long-period seismic signals prior to and during caldera formation on La Réunion Island. Sci. Rep. 9 (1), 1–15.

Gershenzon, N.I., 2019. Instability of frictional sliding. Bull. Seismol. Soc. Am. 109 (3), 1164–1170.

Geshi, N., Shimano, T., Chiba, T., Nakada, S., 2002. Caldera collapse during the 2000 eruption of Miyakejima Volcano, Japan. Bull. Volcanol. 64 (1), 55–68.

Green, D.N., Neuberg, J., 2006. Waveform classification of volcanic low-frequency earthquake swarms and its implication at Soufrière Hills Volcano, Montserrat. J. Volcanol. Geotherm. Res. 153 (1–2), 51–63.

Gudmundsson, M.T., Jónsdóttir, K., Hooper, A., Holohan, E.P., Halldórsson, S.A., Ófeigsson, B.G., et al., 2016. Gradual caldera collapse at Bárdarbunga volcano, Iceland, regulated by lateral magma outflow. Science 353 (6296), aaf8988. https://doi.org/10.1126/science.aaf8988.

Holohan, E.P., Schöpfer, M.P.J., Walsh, J.J., 2015. Stress evolution during caldera collapse. Earth Planet. Sci. Lett. 421, 139–151. https://doi.org/10.1016/j.epsl.2015.03.003.

Hotovec-Ellis, A.J., Jeffries, C., 2016. In: Near Real-Time Detection, Clustering, and Analysis of Repeating Earthquakes: Application to Mount St. Helens and Redoubt Volcanoes – Invited, Presented at Seismological Society of America Annual Meeting, Reno, Nevada, 20 Apr.

Kilburn, C.R., 2003. Multiscale fracturing as a key to forecasting volcanic eruptions. J. Volcanol. Geotherm. Res. 125 (3–4), 271–289.

Kilburn, C.R., Voight, B., 1998. Slow rock fracture as eruption precursor at Soufriere Hills volcano, Montserrat. Geophys. Res. Lett. 25 (19), 3665–3668.

Kobayashi, T., Ohminato, T., Ida, Y., 2003. Earthquakes series preceding very long period seismic signals, observed during the 2000 Miyakejima volcanic activity. Geophys. Res. Lett. 30, 1423. https://doi.org/10.1029/2002GL016631.

Kumagai, H., Ohminato, T., Nakano, M., Ooi, M., Kubo, A., Inoue, H., Oikawa, J., 2001. Very-long-period seismic signals and caldera formation at Miyake Island, Japan. Science 293 (5530), 687–690. https://doi.org/10.1126/science.1062136.

Main, I.G., 1999. Applicability of time-to-failure analysis to accelerated strain before earthquakes and volcanic eruptions. Geophys. J. Int. 139 (3), F1–F6.

Main, I.G., 2000. A damage mechanics model for power-law creep and earthquake aftershock and foreshock sequences. Geophys. J. Int. 142 (1), 151–161.

McGuire, W.J., Kilburn, C.R.J., 1997. Forecasting volcanic events: some contemporary issues. Geol. Rundsch. 86, 439–445. https://doi.org/10.1007/s005310050152.

Michon, L., Staudacher, T., Ferrazzini, V., Bachèlery, P., Marti, J., 2007. April 2007 collapse of Piton de la Fournaise: a new example of caldera formation. Geophys. Res. Lett. 34 (21). https://doi.org/10.1029/2007GL031248.

Minakami, T., Ishikawa, T., Yagi, K., 1951. The 1944 eruption of volcano Usu in Hokkaido, Japan. Bull. Volcanol. 11 (1), 45–157.

Neal, C.A., Brantley, S.R., Antolik, L., Babb, J.L., Burgess, M., Calles, K., et al., 2019. The 2018 rift eruption and summit collapse of Kīlauea Volcano. Science 363 (6425), 367–374. https://doi.org/10.1126/science.aav7046.

Roche, O., Druitt, T.H., Merle, O., 2000. Experimental study of caldera formation. J. Geophys. Res., Solid Earth 105 (B1), 395–416. https://doi.org/10.1029/1999JB900298.

Ruch, J., Acocella, V., Geshi, N., Nobile, A., Corbi, F., 2012. Kinematic analysis of vertical collapse on volcanoes using experimental models time series. J. Geophys. Res., Solid Earth 117 (B7).

Salvage, R.O., Neuberg, J.W., 2016. Using a cross correlation technique to refine the accuracy of the failure forecast method: application to Soufrière Hills volcano, Montserrat. J. Volcanol. Geotherm. Res. 324, 118–133.

Shelly, D.R., Thelen, W.A., 2019. Anatomy of a caldera collapse: Kīlauea 2018 summit seismicity sequence in high resolution. Geophys. Res. Lett. 46 (2). https://doi.org/10.1029/2019GL085636.

Shiro, B., Burgess, M.K., Chang, J.C., Dotray, P., Okubo, P., Thelen, W.A., Montgomery-Brown, E.K., 2018. Earthquake sequences of the 2018 Kilauea Volcano eruption. In: AGU Fall Meeting Abstracts.

Simkin, T., Howard, K.A., 1970. Caldera collapse in the Galápagos Islands, 1968. 1970 Science 169 (3944), 429–437.

Sornette, D., Helmstetter, A., Andersen, J.V., Gluzman, S., Grasso, J.R., Pisarenko, V., 2004. Towards landslide predictions: two case studies. Phys. A, Stat. Mech. Appl. 338 (3–4), 605–632.

Staudacher, T., Ferrazzini, V., Peltier, A., Kowalski, P., Boissier, P., Catherine, P., et al., 2009. The April 2007 eruption and the Dolomieu crater collapse, two major events at Piton de la Fournaise (La Réunion Island, Indian Ocean). J. Volcanol. Geotherm. Res. 184 (1–2), 126–137.

Tárraga, M., Carniel, R., Ortiz, R., García, A., 2008. The failure forecast method: review and application for the real-time detection of precursory patterns at reawakening volcanoes. Developm. Volcanology 10, 447–469.

Tepp, G., Hotovec-Ellis, A., Shiro, B., Johanson, I., Thelen, W., Haney, M.M., 2020. Seismic and geodetic progression of the 2018 Kilauea summit caldera collapse. Earth Planet. Sci. Lett. 540, 116250. https://doi.org/10.1016/j.epsl.2020.116250.

Uchida, N., Bürgmann, R., 2019. Repeating earthquakes. Annu. Rev. Earth Planet. Sci. 47, 305–332.

Voight, B., 1988. A method for prediction of volcanic eruptions. Nature 332 (6160), 125.

Voight, B., Cornelius, R.R., 1991. Prospects for eruption prediction in near real-time. Nature 350 (6320), 695–698.

Zúñiga, F.R., Wyss, M., Scherbaum, F., 1988. A moment-magnitude relation for Hawaii. Bull. Seismol. Soc. Am. 78 (1), 370–373.